Experimental study of rough spherical Couette flows: Increasing helicity toward a dynamo state

Rubén E. Rojas [*] and Artur Perevalov [†]
Department of Physics, Institute for Research in Electronics and Applied Physics, University of Maryland, College Park, Maryland 20742, USA

Till Zürner [‡]
Institut des Sciences de la Mécanique et Applications Industrielles (IMSIA), ENSTA-ParisTech/CNRS/CEA/EDF/Institut Polytechnique de Paris, 91120 Palaiseau, France

Daniel P. Lathrop [§]
Department of Physics, Department of Geology, Institute for Physical Science and Technology, and Institute for Research in Electronics and Applied Physics, University of Maryland, College Park, Maryland 20742, USA

(Received 1 December 2020; accepted 17 February 2021; published 22 March 2021)

We present results of torque and velocity measurement of a 40-cm spherical Couette flow experiment with rough boundaries and compare them with previous work done for smooth boundaries. Spherical Couette flows in liquid metals are a suitable candidate for generating magnetic dynamo states in the laboratory. However, previous work in our 3-m spherical Couette flow experiment and numerical simulation have shown that an enhancement of the poloidal flows and the helicity are likely required to lower the threshold to achieve dynamo action. Finke and Tilgner [Phys. Rev. E **86**, 016310 (2012)] suggested roughening the inner sphere boundary by adding baffles in order to achieve these goals. We perform hydrodynamic studies of the effect of three baffle designs: straight (symmetric) and two types of chevronlike (asymmetric) baffles. In addition, we test the effect of baffle height with two variants: 5% and 10% radius height. We observe important differences in the dimensionless torque as a function of the Reynolds and Rossby numbers for these different configurations and explore an asymmetry in the torque with asymmetric baffles. Velocity measurements in both the equatorial and the meridional planes show an effective enhancement of the equatorial jet and the poloidal flows when adding baffles and two different flow topologies for asymmetric baffles in concordance with the torque measurements. Results point to one of the chevronlike baffle designs as a promising upgrade that we will use in our 3-m experiment to effectively increase our chances of obtaining dynamo action.

DOI: 10.1103/PhysRevFluids.6.033801

I. INTRODUCTION

Rotating flows are ubiquitous in nature: planets, stars, and galaxies exhibit highly turbulent rotating flows in their oceans, atmospheres, and cores. Spherical Couette flows, which are flows between two concentric spheres that rotate differentially, are a useful model to study rotating

[*] rrojasg@umd.edu
[†] pereval@umd.edu
[‡] till.zuerner@ensta-paris.fr
[§] lathrop@umd.edu

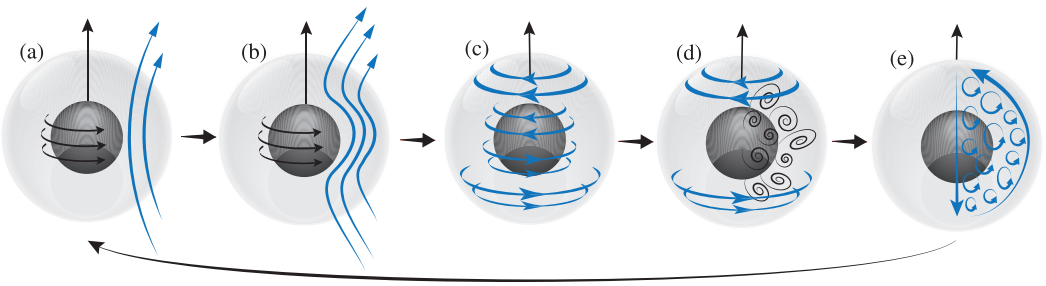

FIG. 1. Schematic representation of the α-ω dynamo. An applied external magnetic field (blue arrows) (a) gets stretched by a differential rotation (b) in the azimuthal direction of the experiment (c), then turbulent and helical flows (d) twist the magnetic field lines back in the direction of a dipole (e), which is the direction of the original applied magnetic field (a), closing the cycle for the amplification process. Adapted from a diagram in [25].

turbulence, particularly in the context of planetary cores [1–3]. Shear forces at the boundaries, and Coriolis forces due to the global rotation drive and shape the motion of the fluid between the spheres, similarly to the more widely explored cylindrical Taylor-Couette flows [2,4–8]. The fluid dynamics resulting from these forces can be used to model various complex phenomena that occur in nature. An example of these phenomena is the self-sustained magnetic field generation seen in many planets due to rotating turbulence of their liquid metal cores, known as the dynamo effect.

Dynamo magnetic field generation can be thought of as a competition between Faraday induction and dissipation due to electrical resistance. The former drags, stretches, twists, and amplifies the magnetic field, while the latter transforms the electric currents into heat at smaller scales. Even though dynamos have been simulated and studied numerically before [9–13], there is a global attempt to replicate Earth-like magnetic field dynamos in the laboratory [14–17], particularly with realistic turbulence that cannot be achieved by current simulations.

At the University of Maryland we built a 3-m-diameter spherical Couette experiment (3 m) [14,18,19], which despite matching many parameters of the Earth's core, has not yielded a magnetic dynamo. The experiment has shown an amplification of the magnetic field in the azimuthal direction up to eight times the externally applied magnetic fields, and amplification of 10%–30% in the radial direction [14].

Theoretical dynamo studies [20,21] indicate that electrically conductive flows can drag and stretch the external magnetic field back into the original applied direction, closing the loop for the feedback process. The amplification of the field observed in the 3-m experiment in the radial direction is evidence of this effect. Flows in the meridional directions [(r, θ)] of the experiment may be responsible for dragging the field into this direction (see Fig. 1 and Sec. II). In Couette flows, energy and angular momentum are injected into the fluid through the boundary layers. Adding roughness to the inner sphere changes the boundary layer from viscous coupling to fully pressure dominated [22–24], which provides a more effective transfer of angular momentum to the fluid and could favor injection of flow in the meridional directions.

Numerical work by Finke and Tilgner [24] examines this directly. In their work, a rough inner sphere, modeled using a body force, was simulated numerically. They found that such body force increases the coupling between the inner sphere and the fluid, resulting in a stronger equatorial jet, therefore increasing the poloidal flows. This new configuration lowers the threshold in the parameter space for achieving dynamo action by a factor of approximately 5. In order to better examine this process before performing long-lasting modifications in the 3-m experiment, we decided to work in a smaller water experiment to study the hydrodynamical properties of spherical Couette flows with and without rough boundaries.

In the present study we a built a 40-c-diameter spherical Couette experiment filled with water. To add roughness we test baffles attached to the inner sphere from pole to pole, in a similar way

as done previously in Taylor-Couette flows [6,23]. Additionally, we try several heights and shapes of baffles to contrast their different effects on the dynamics of the flows. Results include torque measurements from the inner motor as a function of Reynolds and Rossby numbers (Sec. V A), and velocimetry using particle tracers and particle image velocimetry (PIV) in both the equatorial and meridional planes (Sec. V B). One of the goals is to extrapolate these results into the parameter space of the 3-m experiment to guide its redesign; however, we found important properties in the dynamics of rough spherical Couette flows and compared them with previous numerical simulations and experiments, including in Taylor-Couette flows.

These results will allow us to plan modifications in our 3-m experimental setup, not only regarding inner motor power specifications but also final baffle design to move us effectively closer to the dynamo threshold.

II. BACKGROUND

In this section we describe in more detail the dynamo process and list some of the previous laboratory dynamo experiments including more details about the 3-m experiment and forthcoming plans.

The process of dynamo magnetic field generation is a competition between amplification due to Faraday induction and dissipation. The dissipation processes act on both the fluid velocity and the magnetic field. They are determined, respectively, by the momentum diffusivity ν (kinematic viscosity) and the magnetic diffusivity η (inversely proportional to the electrical conductivity). The ratio of these two numbers is known as the magnetic Prandtl number $\mathrm{Pr}_m = \nu/\eta$, and is small for all liquid metals. The Reynolds numbers are also important for understanding the magnetic field generation. The fluid Reynolds number quantifies the ratio of inertial forces to momentum diffusion $\mathrm{Re} = UL/\nu$, where U and L are a characteristic velocity and length scales in the experiment. The magnetic Reynolds number quantifies the ratio of Faraday induction to magnetic diffusion $\mathrm{Rm} = UL/\eta$ (see Sec. IV). The magnetic Prandtl number is also the ratio of these two numbers: $\mathrm{Pr}_m = \mathrm{Rm}/\mathrm{Re}$.

Numerical simulations show a threshold in Rm and Re for dynamo generation in spherical Couette flows [21,24]. For the Pr_m of liquid metals (around 10^{-5}) high Reynolds numbers are required. Such conditions can only be achieved in experimental models, since numerical simulations tend to require $\mathrm{Pr}_m \sim 1$, and thus lack realistic levels of turbulence.

Dynamos have been found in the laboratory in restricted geometries like the ones of Riga [26] and Karlsuhe [27]. These successes proved theoretical predictions about a self-excitation in the magnetic field due to a well organized flow, and motivated the search of dynamos in less confined, more Earth-like geometries and turbulence like in spherical Couette flows. Spherical experiments attempting Earth-like dynamos and exploring magnetoturbulence include the one in Madison at the University of Wisconsin, USA [15] and the DTS spherical Couette flow in Grenoble, France [16,17]. Other experiments, such as the von Kármán sodium experiment [28] and the DRESDYN experiment in Dresden, Germany [29] use a cylindrical geometry. The former successfully achieved a dynamo using ferromagnetic impellers as the main driver of the flow.

The 3-m-diameter spherical Couette experiment at the University of Maryland is intended to mimic the aspect ratio of the Earth's core of $\Gamma = r_i/r_o = 0.35$, where $r_i = 0.51$ m and $r_o = 1.46$ m are the inner and outer sphere radii of the experiment. The boundaries of both spheres are currently smooth with only a characteristic roughness due to the unpolished stainless-steel material from fabrication. The 3-m experiment approximately matches Earth's magnetic Reynolds numbers of $\mathrm{Rm} \approx 900$, $\mathrm{Re} \approx 10^9$, and works with liquid sodium, which has a $\mathrm{Pr}_m \approx 10^{-5}$. An external dipolar or quadrupolar magnetic field can be applied by electromagnets in the axial direction, with an intensity up to 200 G at the center of the experiment. Dynamo action may be excited by the turbulent flows between the spheres. The realignment of the field lines in the originally applied direction would then happen, either at the forcing scale or at the dissipative scales of the flow, allowing the completion of the feedback process amplifying and sustaining the original magnetic field.

One fundamental model for this process is known as the $\alpha\omega$ dynamo [30–32] shown schematically in Fig. 1: a magnetic field is stretched in the azimuthal direction due to shear forces in the form of differential rotation (Ω effect) and then twisted back into the meridional directions due to the helical component of the turbulence (α effect). For the purpose of this paper, we interpret meridional flows as an indicator of the strength of the three-dimensional *poloidal* flows. The turbulence responsible for the α effect can be connected with the vorticity of the meridional flows, which combined with the azimuthal flows responsible for the Ω effect, give rise to helicity. The total helicity is defined as $H = \int_V \boldsymbol{u} \cdot (\boldsymbol{\nabla} \times \boldsymbol{u}) dV$, where $\boldsymbol{u}$ is the velocity vector, and the integral is performed over the fluid volume. In the $\alpha\omega$ dynamo then, the helicity is dominated by the vorticity from the poloidal/meridional flows:

$$H \approx \int_V \boldsymbol{u}_\varphi \cdot (\boldsymbol{\nabla} \times \boldsymbol{u}_m) dV = \int_V u_\varphi \omega_\varphi dV, \tag{1}$$

where the subindexes φ and m stand for azimuthal direction and the meridional plane, respectively, and $\boldsymbol{\omega} = \boldsymbol{\nabla} \times \boldsymbol{u}$ is the vorticity.

Many authors have elaborated on the key role played by the helicity in dynamo action. In particular, Nakajima and Kono [33] proposed that maximizing helicity is strongly correlated with the efficiency of a flow in producing dynamo action. Love and Gubbins [34] and Khalzov *et al.* [35] commented on the connection between helicity and the ratio of poloidal to rotational motion and its influence on the dynamo instability. Further studies support these notions in different flows and geometries [36–41]. Previous results in the 3-m experiment indicated a substantial Ω effect but a limited α effect [14]. Hence, increasing the meridional flows and their vorticity, together with the azimuthal flows, would be an effective way of achieving more helical flows in the experiment, thus enhancing the α effect.

III. EXPERIMENT DESCRIPTION

The experiment shown in Fig. 2 consists of two independently rotating spheres with $\Gamma = r_i/r_o = 0.35$. The 40-cm-diameter outer sphere is made of two 5-mm-thick acrylic shells bolted together at the equator using a rubber gasket seal, and is rotated by a motor using a gear belt. The 14-cm-diameter inner sphere is connected directly to a motor using a shaft that sits on a bearing in the bottom of the outer sphere. Once assembled, the outer sphere is filled with water at about 20 °C. Very extended running times are avoided to reduce changes in temperature: only ± 2 °C were detected, which implies around 0.5% change in kinematic viscosity of the water. This is negligible compared to the experiment systematic uncertainty associated with the friction in the motor (see Sec. V A).

The inner spheres with baffles were 3D-printed from Polylactic Acid (PLA) plastic with baffles whose height was 5% and 10% of the inner sphere radius. Three baffle designs are tested in both heights: straight baffles from pole to pole [Fig. 3(b)], chevron-shaped baffles with a curve given by $\theta = \varphi$ in spherical coordinates on the surface of the sphere [Fig. 3(c)], and a hybrid of straight and chevron baffles as shown in Fig. 3(d), which will be called *alpha* baffles for the rest of this work. The motivation for this design is to test an asymmetric baffle model more amenable to fabrication than the chevron-shaped baffles. With these chevron and alpha designs we aim to break one symmetry of the experiment ($\varphi \to -\varphi$). For smooth and straight design, reversing the rotation direction of both spheres gives the same flow states, whereas reversing both for chevron and alpha designs should yield distinct states. We call these two different modes of operation for each of the asymmetric designs *wedge* and *scoop*. This causes an effective doubling of the parameter space as we will discuss in Sec. IV B.

For the smooth inner sphere, the maximum rotation rate was 50 Hz for the inner sphere and 5 Hz for the outer sphere. We record the current and voltage in the inner motor, calculate the power with these two values, and use the rotation rate to derive the power and torque: $P_i = \boldsymbol{\Omega}_i \cdot \boldsymbol{\tau}_i$, where P_i is the power, $\boldsymbol{\Omega}_i$ is the inner sphere angular velocity, and $\boldsymbol{\tau}_i$ is the torque from the inner motor. Optical

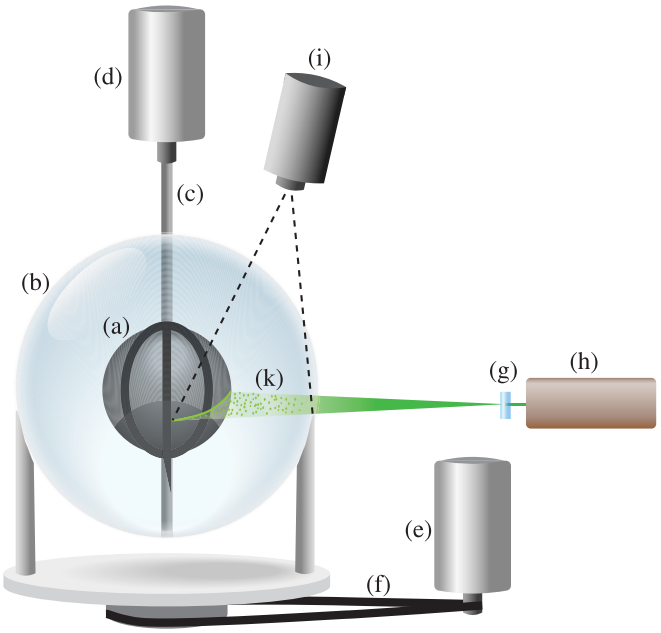

FIG. 2. Schematic of the 40-cm experiment. (a) 12-cm-diameter inner sphere with straight baffles. The baffle height adds 5% or 10% to the inner sphere radius. (b) 40-cm-diameter acrylic outer sphere filled with water. (c) 1-cm-diameter inner shaft. (d) 3-kW inner motor. (e) 2.23-kW outer motor. (f) Gear belt. (g) Cylindrical lens for laser sheet. (h) 6-W $NdYVO_4$ continuous laser. (i) High-speed camera positioned for measurements in the equatorial plane. (k) Polystyrene particles dispersed in the water.

sensors are used to measure the frequency for both motors. The main source of torque error is the friction from the bearings and in the motors. Runs at very low rotation rate are performed to estimate the friction error in the experiment. A run with air instead of water was also performed to examine the error in the torque at high rotation rates.

For the velocimetry measurements a 6-W laser, stationary in the laboratory frame of reference, passes through a cylindrical lens to create a laser sheet. When measurements of the equatorial plane are performed the laser sheet hits the sphere in a parallel plane to the equator a few millimeters above it to avoid being occluded by the flange and gasket seal. Polyethylene fluorescent particles of 75–106 μm diameter are added to the water to allow PIV techniques [42]. High-speed videos at 1000 frames per second (fps) are used to record the particle motions in 1-s intervals. Several videos of the same parameters are performed and averaged.

(a) Smooth (b) Straight (c) Chevron (d) Alpha

FIG. 3. Four types of inner spheres were tested in the 40-cm experiment. The two rotation directions for (c) and (d) are called wedge mode and scoop mode.

To compensate for the spherical aberration due to the change in the refraction index between water and air, a calibration measurement is done as follows: (i) with the camera in the same position as it was for the measurements, a metallic square mesh of known spacing is placed in the equatorial and meridional planes, respectively. (ii) The sphere is filled with water and pictures of both planes are taken. (iii) A nonlinear calibration curve is fitted to the data, which allows us to transform from pixel position in the videos, to radial and angular position in spherical coordinates. In spite of this calibration, spherical aberration makes measurements unavailable near the outer sphere boundary as well as near the shaft and inner sphere boundary due to laser reflections which locally saturate the camera. More details about the velocity measurements will be discussed in Sec. V B.

IV. DIMENSIONLESS PARAMETERS

A. Flow dimensionless parameters

We define the fluid and magnetic Reynolds numbers as

$$\mathrm{Re} = \frac{|\Omega_i - \Omega_o|(r_i - r_o)^2}{\nu}, \quad \mathrm{Rm} = \frac{|\Omega_i - \Omega_o|(r_i - r_o)^2}{\eta}, \tag{2}$$

where Ω_i is the angular frequency of the inner sphere, Ω_o the angular frequency of the outer sphere, and r_i and r_o are the inner and outer radii, respectively. The value for r_i does not include the baffles height. The kinematic viscosity ν is taken as 1.1×10^{-6} m^2/s for water [45] and 0.71×10^{-6} m^2/s for sodium [46]. The magnetic diffusivity η is 0.079 m^2/s for sodium [46].

The dimensionless parameter used to characterize the differential rotation is the Rossby number:

$$\mathrm{Ro} = \frac{(\Omega_i - \Omega_o)}{\Omega_o}. \tag{3}$$

This also indicates the ratio of inertial to Coriolis forces.

We also define the Ekman number as

$$E = \frac{\nu}{\Omega_o(r_i - r_o)^2}. \tag{4}$$

This indicates the ratio of viscous to Coriolis forces. For the 3-m experiment we achieve $E \approx 10^{-9}$, a relatively small number for a laboratory experiment, though still larger than that for the Earth's $E \approx 10^{-15}$ [44].

B. Parameter space

In Fig. 4 we compare the parameter space for the 40-cm, 3-m experiment and a numerical simulation by Wicht [43]. The simulation by Finke and Tilgner [24] is performed with a stationary outer sphere so $\mathrm{Ro} = \infty$ or $E^{-1} = 0$, and does not appear in this figure.

In Fig. 5 we see a representation of the differences in the parameter space due to an asymmetric baffle design like the chevron or alpha baffles [see Fig. 3(c)]. Changing the rotation direction of the inner sphere Ω_i, changes the leading edge shape of the baffles that engages with the fluid. We called these two different directions wedge mode and scoop mode, as indicated in Fig. 5. These two modes are expected to change the hydrodynamics of the resulting flows, hence giving rise to different states, in a similar way that changes in the angle of attack in aerodynamics result in different lift and drag forces for planes [47]. Doubling the parameter space and creating different types of spherical Couette flows may result in increasing our ability to find a dynamo in the 3-m experiment. An initial understanding of the effects of these two modes and its comparison with symmetric baffle designs is then a crucial goal of the present work.

V. RESULTS

The basic driving mechanisms in the experiment are the rotation rates of the inner and outer spheres. Equivalently, we can use Reynolds and Rossby numbers as independent control parameters:

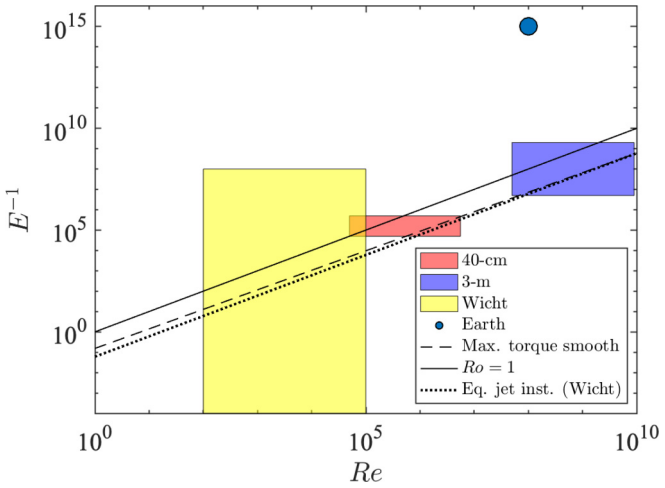

FIG. 4. Inverse Ekman and Reynolds number parameter space for experiments (40 cm, 3 m), simulations (Wicht [43]), and the Earth [44]. A solid line for Ro = 1 is shown for reference. The dotted line indicates the equatorial jet instability regime as observed by Wicht. The dashed line indicates the maximum torque line for a smooth inner sphere observed in the present work and in Zimmerman *et al*. [14].

the former measures the turbulence due to the differential rotation, and the latter measures the importance of the overall rotation. These parameters have been previously used to map the dynamics of Taylor and spherical Couette flows [14,48].

We separate the results into two sections: first, we show torque as a function of Reynolds and Rossby numbers. Then, we show PIV results performed in both the equatorial and meridional planes to examine flow differences for each baffle design.

A. Torque measurements

We define the dimensionless torque as

$$G = \frac{\tau}{\rho \nu^2 r_i}, \tag{5}$$

where τ is the dimensional torque, ρ the fluid density, ν the kinematic viscosity, and r_i the inner sphere radius. Similarly, we define G_∞ as the dimensionless torque when Ro $= \infty$; i.e., when the

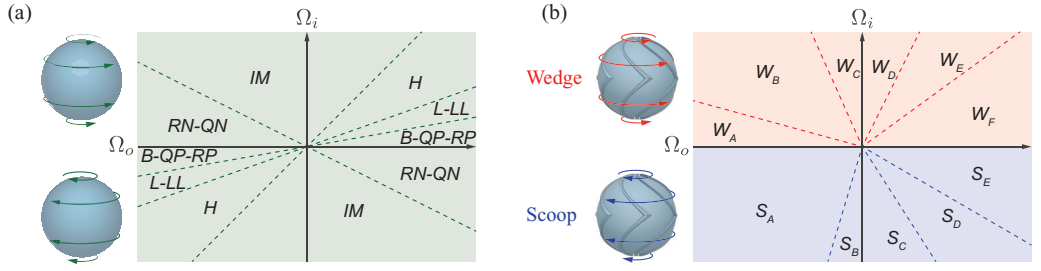

FIG. 5. Schematic of the doubling of the parameter space (Ω_o, Ω_i) by breaking the symmetry of the inner sphere with respect to the rotation direction. The Finke and Tilgner [24] parameter space corresponds to the vertical axis. In (a) an inversion with respect to the origin results in the same states, making this plane symmetric to inversion through the origin. In (b), an inversion results in different, yet unknown, states. State labels for (a) come from prior studies in the 3-m system [14]. State labels in (b) are for illustrative purposes only.

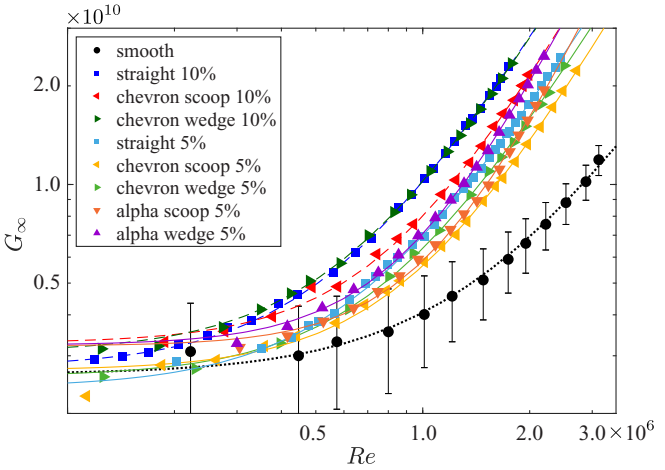

FIG. 6. Dimensionless torque from the inner motor versus Reynolds number with stationary outer sphere (Ro $= \infty$) for all baffle designs. A power law of the form $G_\infty = b\,\mathrm{Re}^a + c$ was fitted to each data set. Values a, b, and c are listed in Table I. Dotted, dashed, and solid curves indicate no baffle, 10%, and 5% baffle height designs, respectively. Smooth design error bars are shown for reference and apply for all curves.

outer sphere is stationary. This parameter will be important later when we use it to normalize the dimensionless torque as a function of differential rotation.

1. Reynolds number dependence

The Reynolds number dependence of the dimensionless torque with a stationary outer sphere [G_∞(Re)] is shown in Fig. 6 for all three baffle designs (as well as no baffles: smooth) and two baffle heights in the 40-cm experiment. We distinguished between scoop and wedge modes in both the chevron and alpha designs. As expected, the 10% baffles present a higher torque than the 5% ones. Additionally, we see that wedge mode [(see Fig. 5(b)] generates more torque than scoop for both baffle heights and both asymmetric designs (chevron and alpha). The reason for this will become clearer when we examine the velocimetry data in Sec. V B 2.

We have fitted a power law of the form $G_\infty = b\,\mathrm{Re}^a + c$ to the dimensionless torque over the entire range of Reynolds numbers measured. The resulting coefficients are shown in Table I. We

TABLE I. Power-law fit of the form $G_\infty = b\,\mathrm{Re}^a + c$ of the plots in Figs. 6 and 7 and Taylor-Couette flows in [48].

Experiment	a	b	c
3 m ($\Gamma = 0.35$) [14]	1.89	0.003	3.3×10^{10}
Smooth	1.58	0.044	2.6×10^{9}
Straight 10%	1.77	0.18	2.8×10^{9}
Chevron scoop 10%	1.80	0.11	3.1×10^{9}
Chevron wedge 10%	1.95	0.0093	3.3×10^{9}
Straight 5%	1.74	0.16	2.4×10^{9}
Chevron scoop 5%	1.81	0.047	2.6×10^{9}
Chevron wedge 5%	1.89	0.012	2.7×10^{9}
Alpha scoop 5%	2.11	0.00068	2.7×10^{9}
Alpha wedge 5%	2.17	0.00035	3.2×10^{9}
Taylor-Couette ($\Gamma = 0.72$) [48]	1.85	0.03	1.0×10^{8}

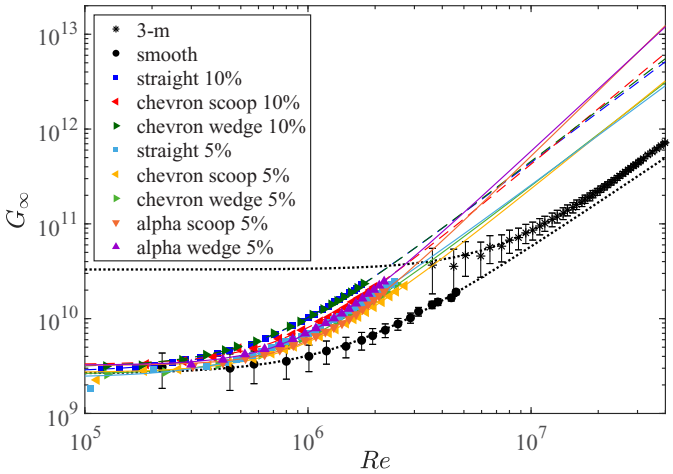

FIG. 7. Same for Fig. 6 but we extrapolate the power laws of the 40-cm experiment to higher Reynolds numbers in order to compare with 3-m experiment torque data from Zimmerman *et al.* [14] (stars). Dotted, dashed, and solid curves indicate no baffles, 10%, and 5% baffle height designs, respectively. For clarity, we only show error bars for smooth in 40-cm and for the 3-m experiment.

interpret the constant c as a torque due to friction in the shaft's contacts, the motors, and the bearings. As was done for previous works in 3 m [14], this value c was used as total length of the error bars for each plot since at higher rotation rates it does not change significantly and it is still the biggest source of uncertainty.

The exponent a, approaches $a = 2$ (the Kolmogorov scaling) asymptotically for increasing Reynolds number in shear-driven turbulence, as shown in [5,6]. In Table I we observe that for the 40-cm experiment, runs with baffles have higher exponents a than the smooth design, indicating that a tripped boundary layer and pressure drop across the baffles are improving the angular momentum transport. This is well documented by van den Berg *et al.* [6] and Zhu *et al.* [22] in which they showed in a Taylor-Couette experiment how wall roughness facilitates transport until the Kolmogorov scaling (in which viscosity dependence is eliminated) is reached, leading to purely pressure drop dominated flows. It is also important to mention that before the Kolmogorov scaling regime where the exponent converges to 2, there is a transition region where the exponent could be higher than 2 for an intermediate range of Reynolds numbers as is well known in boundary layer theory for the case for rough boundary pipe flows (see, for instance, [49]).

The prefactor b in Table I is a geometry-dependent friction factor associated with the gap between the sphere boundaries as indicated by [14] and it is expected to be lower for wider gaps. The radius ratio for Earth-like spherical Couette is $\Gamma = r_i/r_o = 0.35$ and for Taylor-Couette used in [48] $\Gamma = 0.7245$. We would expect the prefactors b in the 40-cm experiment to be of the same order of 3 m, since the radius ratio is the same, but this is not the case. They all vary between the values of 3 m and Taylor-Couette, straight being higher than scoop, and scoop higher than wedge in each baffle configuration and size. Also, the prefactors in 10% baffles are higher on average than the 5% baffles (except for wedge 10%), which is consistent with [14].

We extrapolate these power laws into the parameter space of the 3-m experiment (Fig. 7) to estimate torque and power demands from these baffle designs, which are important design data. First, we notice that the power law for the smooth case seems to align with that of the 3-m experiment at high Re; although the slope is smaller, the magnitude is very close relative to the other projections. This might indicate that the inner sphere of the 3-m experiment is already affected by its slight roughness that is higher than that of the smooth sphere of the 40 cm. It might also indicate that for the parameters in the 40-cm experiment we have not reached the same regime observed in

TABLE II. Location and amplitude of the maxima in Fig. 8 and Taylor-Couette flows in [48].

Experiment	G/G_∞	Ro^{-1}
3 m ($\Gamma = 0.35$) [14]	1.20	−0.05
Smooth	1.04	−0.07
Straight 10%	2.86	−0.25
Chevron scoop 10%	3.10	−0.25
Chevron wedge 10%	2.27	−0.21
Straight 5%	2.21	−0.16
Chevron scoop 5%	2.13	−0.16
Chevron wedge 5%	1.77	−0.14
Alpha scoop 5%	2.53	−0.14
Alpha wedge 5%	2.23	−0.16
Taylor-Couette ($\Gamma = 0.72$) [48]	1.25	−0.25

the power law for 3 m. [14]. This is consistent with the fact that the exponent a is the lowest among all the designs in 40 cm.

We can see in Fig. 7 that the extrapolated torque for all 10% baffles is approximately eight times bigger than 3 m at $\mathrm{Re} \approx 3.0 \times 10^7$, which is the highest Re recorded for this measurement in 3 m. Also, the extrapolated torque for the chevron and straight 5% baffles at this Re is four times bigger than 3 m. Nevertheless, the 5% height alpha baffles show the highest torque projection among all of them, even compared to the 10% baffles. Since the fitting exponent a is greater than 2 at the 40-cm Reynolds number, it is expected that the projection into 3-m parameter space may be overestimated.

Even though we only have three data points, there seems to be linear proportionality between the torque and the height of the baffles at high Re. This is not the case for Taylor-Couette flows discussed in [23] where the relation between these two parameters seems to be closer to quadratic. A linear dependence is consistent with the increase of surface area of the baffles. However, more measurements for different heights of baffles would be required for a better understanding of the dependence in spherical Couette flows.

2. Rossby number dependence

When we differentially rotate both spheres, the Coriolis forces shape the flow, significantly changing the states. The Rossby number (defined in Sec. IV) characterizes the differential rotation and from past work determines which dynamical state is observed. In order to isolate the dependence of the dynamics on the Rossby number, we normalize the dimensionless torque by G_∞. Previous work by Zimmerman *et al.* [14] and Paoletti and Lathrop [48] found that the torque, for both Taylor-Couette and spherical Couette flows, can be factorized at high Reynolds number ($\mathrm{Re} \approx 10^6$) as

$$G(\mathrm{Ro}, \mathrm{Re}) = f(\mathrm{Ro}) G_\infty(\mathrm{Re}), \tag{6}$$

where $G_\infty(\mathrm{Re})$ is the torque with outer sphere stationary, i.e., $\mathrm{Ro} = \infty$. Then G/G_∞ is a function of Ro only, and the torque G scales like $G_\infty(\mathrm{Re})$ for a fixed $\mathrm{Ro} \neq \infty$.

The form of $G/G_\infty(\mathrm{Re})$ in Fig. 8 is similar to the one in 3 m [14] and in Taylor-Couette flows [48]. The main difference is the amplitude and location of the peaks for maximum relative torque. For 10% chevron scoop and 10% straight baffles the amplitude is more than three times the scaled peak torque in the 3-m system (see Table II for actual values). This shows a much stronger forcing for differential rotation relative to a stationary outer sphere and indicates that the coupling between the spheres is significantly higher with baffles. We can also see that the amplitude of the peak for chevron wedge is the lowest of the 10% baffle designs. This same proportion between these designs prevails for straight and chevron 5%; however, the amplitude changes. This indicates a

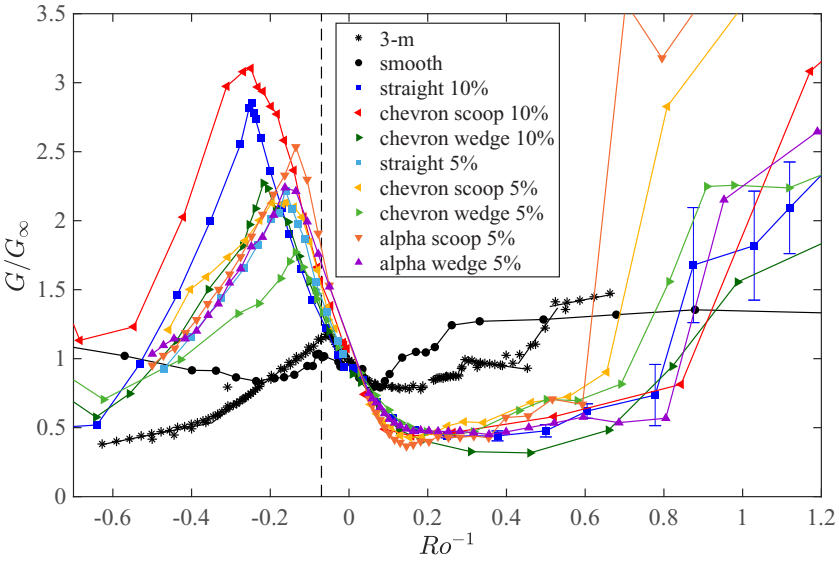

FIG. 8. Rossby number dependence of the measured inner sphere torque. The magnitude of the torque at a given Ro and Re is normalized by G_∞(Re), the torque expected at that Reynolds number if the outer sphere were not rotating. Error bars for straight 10% are shown in the range of bistable states and are representative for all baffles $\mathrm{Ro}^{-1} > 0.6$. The dashed line indicates the location of the peak for maximum relative dimensionless torque in the 40-cm experiment with smooth inner sphere.

lower coupling with lower baffle height, a similar result to that of Taylor-Couette flows [22]. Less obvious are the reasons for the difference in torque between wedge and scoop modes for the same baffle design: the peak amplitude for scoop mode is higher than wedge mode. The same behavior happens for alpha baffles of 5% height, but if compared to the other 5% models, it is higher than all of them. Additionally, alpha scoop 5% is even higher than chevron wedge 10%. This suggests a more effective coupling at the expense of less absolute torque, i.e., a smaller G_∞ for the case of alpha baffles.

Another interesting feature is the location of the relative torque maxima, as can be seen in Table II. It moves to lower inverse Rossby numbers as we increase baffle height. This is expected as indicated in [14,50] where a reduction in the gap would imply an amplification of the fluid engagement, or coupling between the boundaries. With this, a lower rotation rate in the inner boundary is required to match the fluid drag and angular momentum transferred to the fluid from the outer boundary, corresponding to a reduction in the inverse Rossby number. This reduction of the gap also explains why this maximum is located at lower values for spherical Couette versus Taylor-Couette flows. The location of the maximum also changes for wedge versus scoop modes. All of these differences suggest a very rich dynamics happening for different models of baffles that required more than global measurements (like torque) to be described, and that motivated the velocimetry studies in Sec. V B.

For $\mathrm{Ro} > 0$ we observed bistable states that happen between $0.6 < \mathrm{Ro}^{-1} < 1$ in Fig. 8 in the region that also sees a large increase torque. The same behavior happens for all baffle designs. These results are similar in location and amplitude to bistable states in the 3-m experiment that are characterized in more detail in [18]. The time dynamics can be described as a spontaneous jump between two torque values: a slow decay into the lower torque state (named L) followed by a jump into a higher torque state (H). The timing between these states, and the time spent in each one of them, as reported in [14,18], depends highly on the Rossby number. This bistability was more

evident in torque fluctuations with baffles relative to the smooth design, presumably because the engagement of the boundaries with the flow is higher.

B. Velocimetry

In this section we will show results of the velocimetry measurements performed using PIV techniques in the equatorial and meridional plane of our 40-cm spherical Couette apparatus. For the velocimetry in the equatorial plane, we focused on the dependence of the velocity as a function of radius since, by symmetry, we expect certain invariance of the velocity field as a function of the azimuthal angle φ. For our study, we only focused on time averages, so wave motion was not analyzed in our measurements, although the presence of waves in the spherical Couette setup is well known (see, e.g., [51–53]). For the meridional plane we inspected the dynamics at constant Rossby numbers corresponding to the maximum G/G_∞ for reasons we will explain in the next section.

Recordings of 1 s duration were performed using a high-speed camera at 1000 Hz. The rotation rate of the inner sphere is between 10 and 15 Hz around the maximum torque area for all the baffle designs, which means 10–15 rotations of the inner sphere per each 1-s movie taken.

1. Equatorial plane

The dimensionless torque measurements in Sec. V A show very different dynamics for each design as a function of Ro^{-1}, mainly by the location and amplitude of the maximum relative torque peak (see Fig. 8). This point of maximum relative torque has shown the highest amplification of magnetic field in the cylindrical radial direction [14] for the liquid sodium flows. We performed velocimetry for a range of Ro values around the peak with $\mathrm{Re} \approx 10^6$. We normalized the velocities by the tangential velocity of the inner sphere at the equator, $\Omega_i r_i$, where r_i is the radius of the inner sphere, and Ω_i its angular frequency. We also define the normalized radius as $\rho = (r - r_i)/l$, where $l = r_o - r_i = 12$ cm is the gap between the spheres.

In Figs. 9 and 10 we show color plots of the normalized radial velocity as a function of the normalized radius $u_r(\rho)$ and the normalized azimuthal velocity as a function of the normalized radius $u_\varphi(\rho)$. We have also shown in each graph the average velocity only as a function of Ro^{-1}. Additionally, the location of the maxima relative torque for each baffle design (shown in Fig. 8 and listed in Table II) is indicated with a dashed line on each of the plots. Since on average the bistable states occur on a timescale bigger than the camera recording time lapse, we have omitted velocity measurements for the Ro where bistability occurs.

Looking at the smooth case first, we notice that the velocity in the azimuthal direction (see Fig. 10) is much higher on average than the radial velocity (see Fig. 9). Near the region of maximum torque the azimuthal velocity reaches a minimum and there is an equatorial jet radially outward. This equatorial jet strengthens as we approach to the maximum torque peak. The radial velocity seems irregular and fluctuating in comparison to the azimuthal component. This could be due to the low values of the radial velocities compared to the azimuthal velocities, or because of dynamics that are longer term than our 1-s measurements. The Rossby number for the formation of this jet coincides with the Rossby number for the peak of highest amplification of the radial magnetic field in the 3-m system, which reinforces the importance of the mean flows in the amplification process [24].

For the straight 10% baffles, we see a significant increase in the maximum relative radial velocity with respect to the smooth design. This is by itself a very important result: baffles have increased the coupling between the inner sphere and the fluid, resulting in a better radial transfer of angular momentum. We reiterate that the normalization is by the tangential velocity of the inner sphere at the equator, so this increase is not related to the angular velocity of the spheres, rather to the interaction between its boundary and the flow. The equatorial jet seems more stable and uniform here than in the smooth design, and we can see that it spreads out through the entire radius at the peak of maximum torque.

If we compare this last result with Wicht [43] in Fig. 4, we see that the Rossby number for the equatorial jet instability (dotted line) coincides with the Rossby number of maximum torque

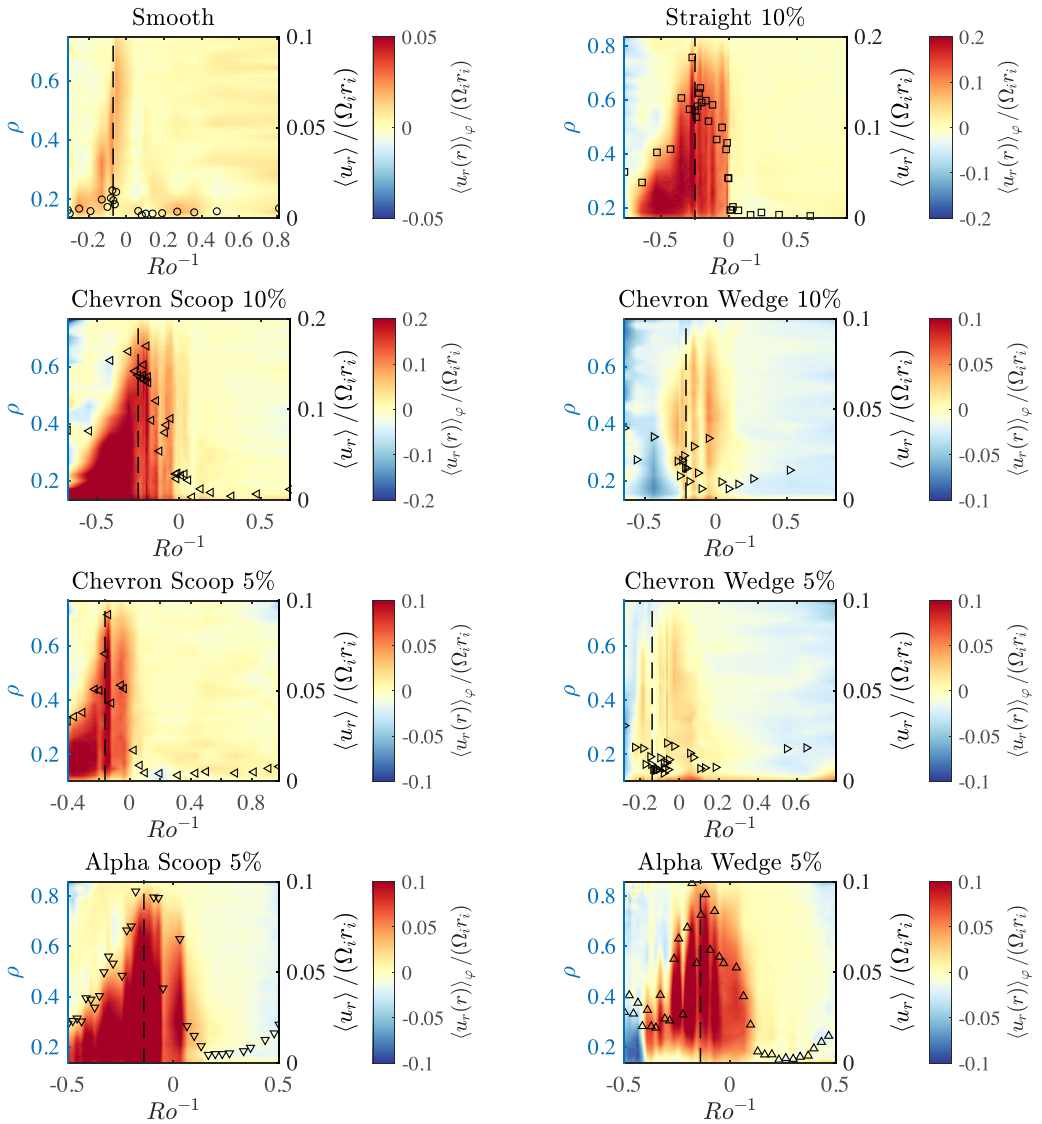

FIG. 9. Radial velocity in the equatorial plane for all baffle designs. In color map: azimuthal average of the velocity in the radial direction, normalized by the tangential velocity at the inner sphere equator, as a function of the normalized radius (left vertical axis) for different Rossby number (horizontal axis). Warm colors mean velocity in the direction outward from the inner sphere and cool colors inward. The symbols show the radial average of each of the columns in the color plot (indicated in the right vertical axis) as a function of Ro^{-1}. The vertical dashed lines indicate the location of the maximum relative torque G/G_∞ for each baffle design.

(dashed line) in the parameter space. We show one Reynolds number in the color plots of this section. Measurements done for different Re confirm that the Rossby number for the maximum torque peak does not change significantly with Re for any of the baffle designs.

For the chevron scoop mode with 10% baffle height, we see that the general behavior and intensities are very similar to straight 10% baffles although the equatorial jet seems more uniform when changing Rossby numbers around the maximum torque peak. This might be due to the baffle orientation: if you see Fig. 5, scoop mode orientation pushes the fluid into the equatorial plane

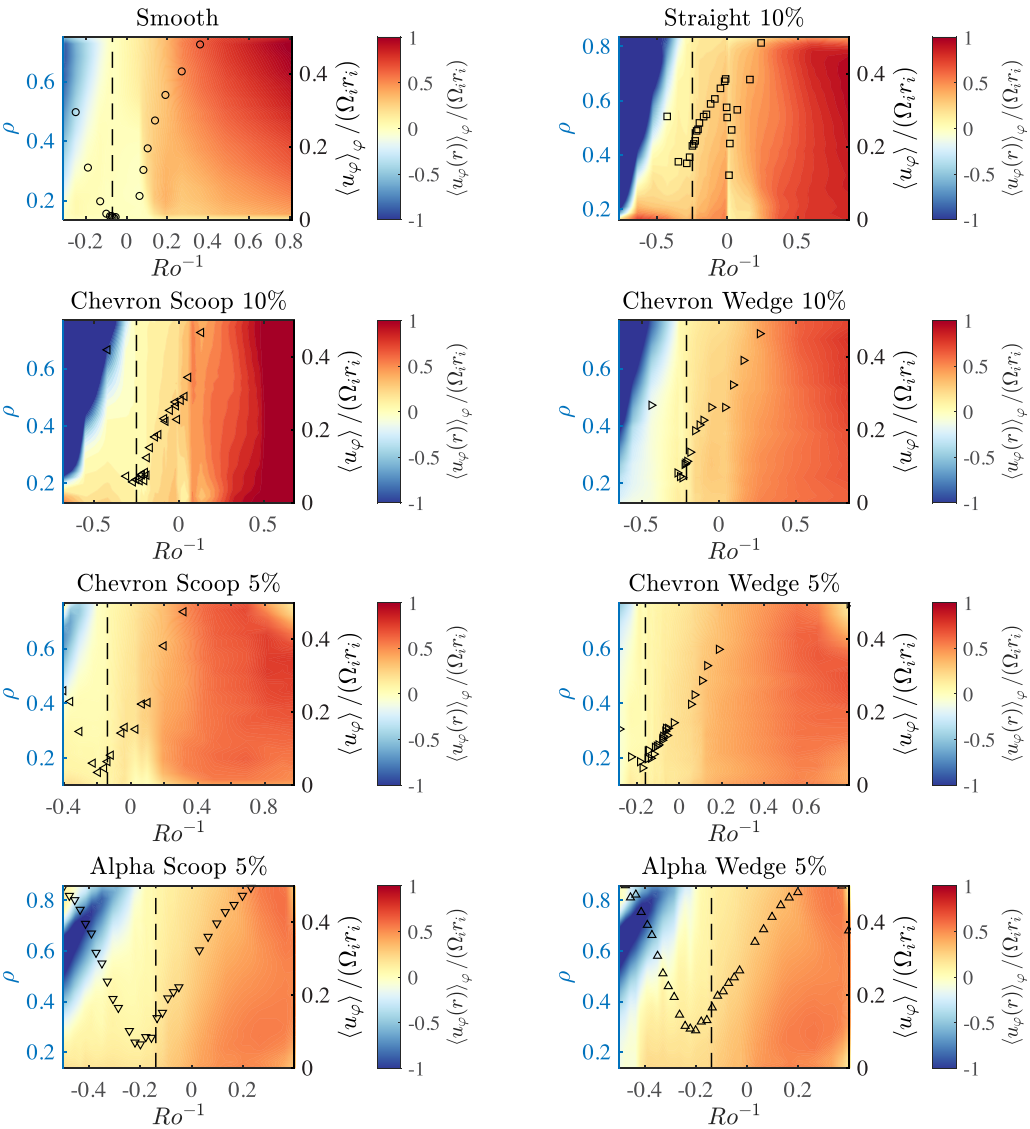

FIG. 10. Azimuthal velocity in the equatorial plane for all baffle designs. In color map: azimuthal average of the velocity in the azimuthal direction, normalized by the tangential velocity at the inner sphere equator, as a function of the normalized radius (left vertical axis) for different Rossby number (horizontal axis). Cool colors mean velocity in the opposite direction of the rotation of the inner sphere and warm colors mean moving in the same direction. The symbols show the radial average of each of the columns in the color plot (indicated in the right vertical axis) as a function of Ro^{-1}. The vertical dashed lines indicate the location of the maximum relative torque G/G_∞ for each baffle design.

due to the inclination of the baffles. Additional data in favor of this hypothesis will be shown in Sec. V B 2. A similar result as in the previous plots is seen for the azimuthal velocity: a lower u_φ for the maximum G/G_∞ and an inner-sphere-dominated dynamics in this region.

For the chevron wedge mode with 10% baffle height, we can see (Fig. 9) that now the radial profile is different from previous ones: the equatorial jet has very low intensity and has spread in the radial direction. It also looks nonuniform and there is a negative inward flow around $\mathrm{Ro}^{-1} \approx -0.5$.

This shows a different dynamics for this mode, with a less stable equatorial jet and timescales slower than 1 s for this regime.

A possible explanation for the lower radial amplitudes is again the orientation of the baffles that now, in wedge mode, push the velocity upward from the equator in the direction of the poles, causing a narrower and weaker equatorial jet. This might be the reason that the absolute torque of the wedge mode is higher than scoop mode (Fig. 6): the orientation of the blades pulls the fluid in the negative radial direction at the equator, creating pressure gradient unfavorable for the equatorial jet that happens due to centrifugal forces. This competition between a centrifugal force and a negative pressure gradient requires more torque in the inner motor, causing the difference in the absolute torque plots.

We now proceed to compare specifically 10% baffles with 5% for the chevron shape, in the second to last row of Figs. 9 and 10. There the velocity profiles are very similar between both baffles heights but the amplitudes are smaller for the 5% height; hence, the coupling has reduced with respect to the 10% baffle design as expected. For wedge mode, the negative circulation and irregularity in the radial flow is again present, and for chevron scoop 5% we also see a well formed and stable equatorial jet around the maximum torque region.

Finally for alpha baffles, the results have the same characteristic peak at maximum torque for the radial velocity with similar amplitudes to the chevron 5% cases, except for the wedge mode, where we can see now a clear jet being formed. However, it seems to be more unstable than the alpha scoop mode, which is consistent with previous wedge baffle results. We can also observe an inward flow in the radial plot around $\mathrm{Ro}^{-1} = -0.5$ as was observed for chevron wedge 10%. For the azimuthal velocity similar behavior to the other baffles and modes is observed, although now the values near the maximum torque, i.e., at the minimum azimuthal velocity, seem to be greater than previous chevron 5% cases, implying that the coupling with the inner sphere is stronger. There seems to be a mismatch between the torque peak (dashed vertical line) and the minimum for azimuthal velocity for alpha baffles. A similar phenomenon was reported by Zimmerman *et al*. [14] in the 3-m experiment, where they noticed that the minimum of Ω effect, i.e., a minimum on the gradient of azimuthal velocity, is offset from the torque maximum peak.

Besides the different dynamics observed for wedge and scoop mode in both chevron and alpha designs, the aforementioned features inspired the results obtained in the next section: near this maximum torque region, the azimuthal velocity reaches a minimum. According to Holme [36] the poloidal shear is at a maximum where the toroidal shear is close to zero, which is consistent with our observations. This motivated us to perform measurements in the meridional plane; a task we thought would be very difficult to achieve due to the high velocities that rotating fluid experiments normally have in the azimuthal direction, i.e., the direction of rotation. With these low azimuthal velocities at the maximum torque region, a laser sheet in the meridional plane could illuminate particles for enough time to be captured by the high-speed camera.

2. Meridional plane

We now present results of the velocity field in the meridional plane ($\varphi = \text{const}$) at a fixed Rossby number equal to the corresponding maximum torque for each baffle design (refer to Table II). Due to the low velocities in the azimuthal direction at this particular region, as shown in the previous section, we could have particle tracks long enough to be detected by the high-speed camera. It is important to mention that this still brings a cutoff for the maximum velocity we can measure: assuming the width of the laser is 3 mm, the camera records at 1000 fps and that we discard tracks shorter than four frames, the maximum speed we can detect is around 1 m/s, which is close to the maximum speed we measured on the meridional plane but high enough to not saturate the plots.

Since we fixed Ro, we did a sweep for different Reynolds numbers to compare the difference in the dynamics. Averages between different Reynolds numbers were performed over the normalized velocity fields only for those states in which the dynamics was similar enough; in our case, for $1 \times 10^6 < \mathrm{Re} < 2 \times 10^6$. Although we only show results for the 5% baffle height designs in this

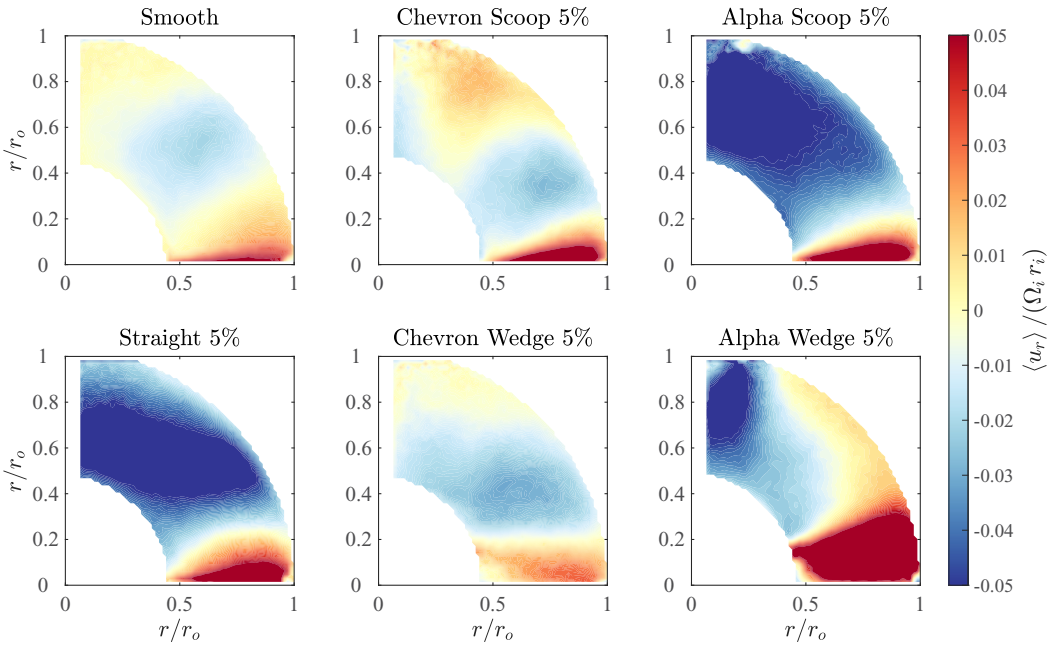

FIG. 11. Spherical radial component of the velocity field (u_r) in the meridional plane (r/r_o, θ) normalized by the tangential speed in the inner sphere at the equator, for different baffle designs and modes. We normalize the radial coordinate by the radius of the outer sphere r/r_o. Warm colors are outward radial flows, and cold colors are inward radial flows.

section, we expect 10% meridional plots to behave similarly but with higher relative velocities given our results comparing 5% and 10% torque and equatorial velocity measurements in previous sections.

In Fig. 11 we can see the spherical radial component of the velocity field (u_r) in the meridional plane, as a function of r and θ, for each baffle design. First, we notice a clear increase in the velocities with straight baffles, the equatorial jet is stronger by a factor of approximately 2 in the bulk of the jet, and there is a broader area of inward flow, or recirculation, above it. The main kinetic energy is stored at the equatorial jet [24,54], so this increase is by itself a favorable result for dynamo action. If we now take a look at the results for the chevron design, we notice that the scoop and wedge modes show different topologies. The radial flows in the chevron scoop mode are similar to smooth and straight with an equatorial jet that is more intense than the smooth case but with less meridional circulation than the straight case. If we now take a look at the chevron wedge mode, we notice the equatorial jet is much weaker here, even weaker than the smooth case, but there is more inward flow above the equatorial jet. This is consistent with the torque plots in Fig. 8 where chevron wedge 5% requires less torque to run at constant speed at maximum Rossby than chevron scoop 5%. It also agrees with the equatorial plots in Fig. 9 that show this difference in the equatorial plane intensities. A very similar result can be observed for the meridional component of the velocity field of the baffle designs mentioned above (smooth, straight, and chevron) in Fig. 12: an increase of the intensities when baffles are added specially with straight baffles and a different topology in the flows for chevron scoop and wedge.

Alpha baffles combine the stronger coupling observed in the straight baffles case, with the change in the topologies due to an asymmetric design [see Fig. 3(d)]. The results are very promising: we can see that the topology and intensities of the scoop mode are very similar to the straight baffles case. For the wedge mode now the equatorial jet in Fig. 11 is much wider and intense than the chevron

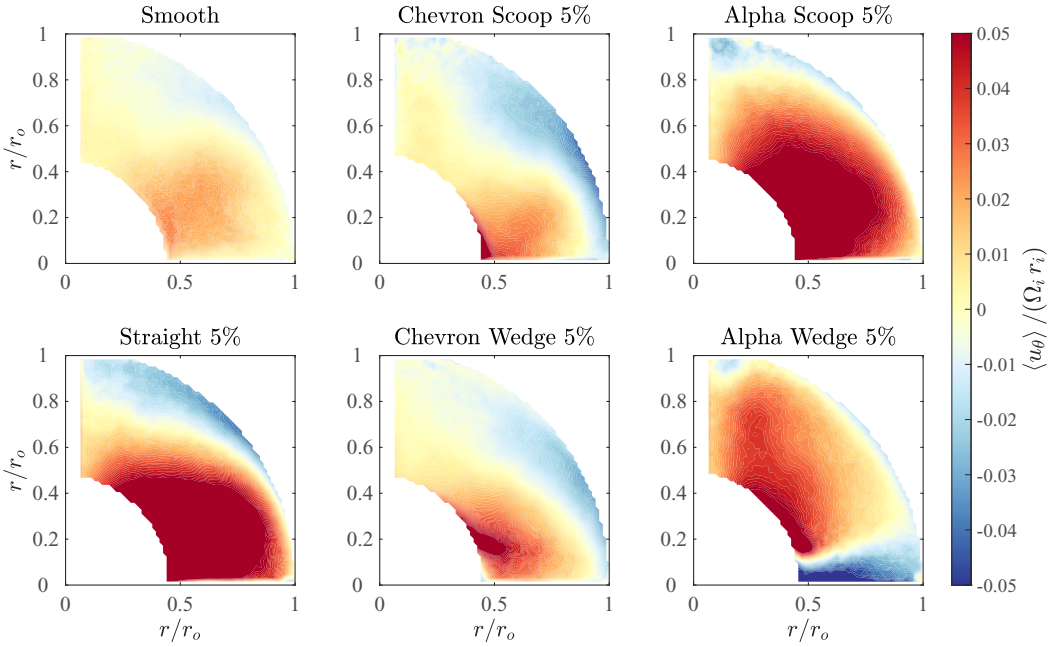

FIG. 12. Meridional component of the velocity field (u_θ) in the meridional plane ($r/r_o, \theta$) normalized by the tangential speed in the inner sphere at the equator, for different baffle designs and modes. We normalize the radial coordinate by the radius of the outer sphere r/r_o. Warm color are flows from the north pole toward the equatorial plane, and cold colors are toward the pole.

wedge mode, with values that are on the same order of magnitude as the scoop mode, with a stronger recirculation. For the meridional flows we now notice a negative region above the equatorial planes, which indicates that the flow is going upward in the bulk of the jet, creating a different topology than the scoop mode. We also notice a thinner recirculation layer near the outer sphere boundary and the shaft. Those recirculation layers likely extend into the region outside the measurement volume. These topologies in the flows are consistent with the interpretation given before about the orientation of the blades and the direction of the flow transported: scoop modes push the flow in the direction of the equatorial plane, amplifying its intensity; however, wedge mode takes it out of the equatorial plane and together with the centrifugal forces, transfers the energy into the meridional directions. With the alpha baffle designs, we will gain similar coupling as with straight baffles while doubling the parameter space like with chevron baffles. This is important for future design considerations in the 3-m experiment.

As mentioned before, the vorticity in the meridional plane, combined with the flows in the azimuthal direction indicate the helicity of the flows in the meridional planes. Figure 13 shows the local vorticity of the flows in the meridional plane for all the baffle designs. The region around the equator for straight, chevron scoop, and alpha scoop with respect to the smooth design, shows a significant increase compared to other regions of the meridional plane. Additionally, the region of high vorticity is wider for chevron wedge and alpha wedge and it is located now at a latitude above the equator, showing even a positive vorticity in the region adjacent to the inner sphere at the equator level. This positive vorticity region is more evident for the alpha wedge mode, and is consistent with the meridional flows in Fig. 12 that show a negative meridional velocity in this region. Such redistribution of the vorticity can be favorable for dynamo action [33], by increasing the α-effect in the 3-m experiment and hence reducing the critical magnetic Reynolds number for dynamo action [34,37,38]. Additionally, according to some authors [55] having a gradient of helicity is an important

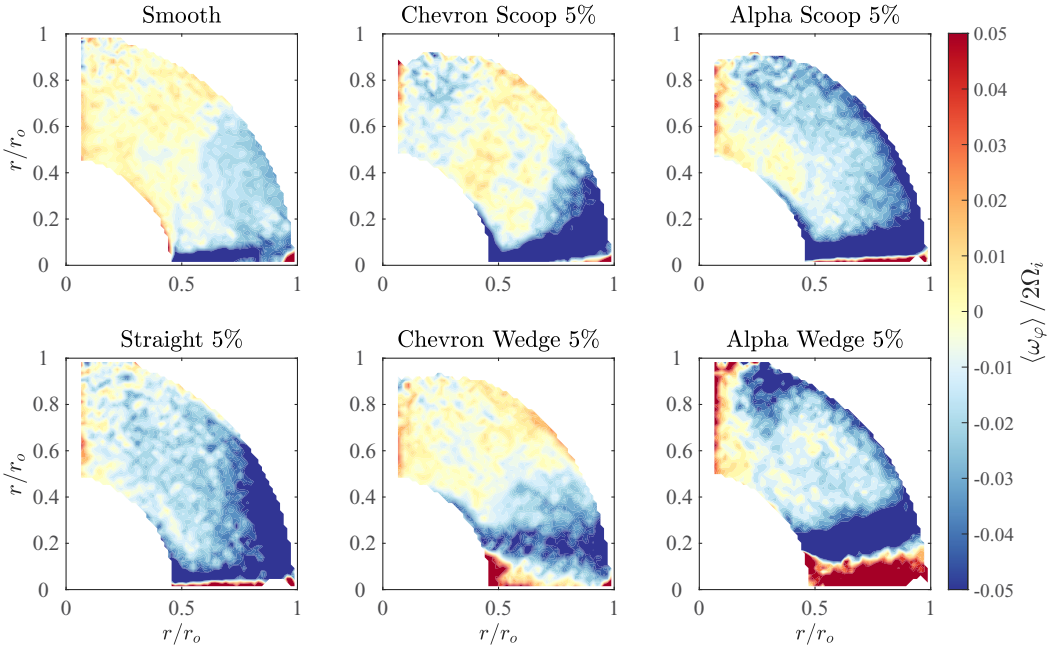

FIG. 13. Local time average azimuthal vorticity normalized by the inner angular frequency in the meridional plane $(r/r_o, \theta)$ for different baffle designs and modes. We normalize the radial coordinate by the radius of the outer sphere r/r_o. Negative values point out of the page.

ingredient for dynamo generation. With alpha wedge baffles we would have a configuration that allows us to explore this effect in the 3-m experiment.

The properties for the vorticity generated by alpha baffles, combined with the highest values for the averaged azimuthal velocity shown in Sec. V B 1, suggest that the alpha design generates the most promising flows for achieving an enhancement of the helicity in the 3-m experiment.

VI. CONCLUSIONS

We present results on torque scaling and velocimetry of spherical Couette flows with rough boundaries and compare them with previous work done for smooth boundaries. For roughening the inner sphere boundary we studied four designs of baffles: smooth (no baffles), straight, chevron, and alpha baffles (Fig. 3) with 5% and 10% of radius height. We observed different power laws in the dimensionless torque as a function of the Reynolds number (Fig. 6) for these different configurations and identified a difference in the torque for counterclockwise and clockwise rotation of the inner sphere with chevron and alpha baffles due to their asymmetry. Additionally, the torque increases with increased baffle height for three different heights (including smooth case), and it shows a linear dependence rather than a quadratic one, as was reported for Taylor-Couette flows [23]. For the Rossby dependence of the torque, we observed a significant increase in the normalized differential torque when adding baffles, which indicates an increase in the angular momentum transport (Fig. 8). The location of the maximum torque peak also changes, not only with the baffle height but also when comparing wedge mode with scoop mode in the case of chevron and alpha baffles. This is evidence of the change in the dynamics of the flows for these two modes. Velocimetry in the equatorial plane (Fig. 9) shows a fully extended equatorial jet that reaches the outer boundary when the torque reaches its maximum relative value. This location in the parameter space matches the equatorial jet instability observed by Wicht [43]. In this region, the azimuthal velocity is at its minimum value throughout all the Rossby numbers measured.

This region of maximum normalized torque seems to be a good candidate for the generation of dynamo action in the 3-m experiment, since it has shown maximum radial amplification of the applied magnetic field [14]. Velocimetry measurements of the meridional section at this maximum torque Rossby number showed a significant amplification of the poloidal flows and these results are in agreement with previous equatorial velocimetry measurements (Figs. 11 and 12). A difference in the topology of the flows generated was observed in both the equatorial and meridional sections. The results from this work may be useful for understanding the changes in the dynamics that will occur in the 3-m experiment when the final modifications are performed. The torque scaling information (Fig. 7) in particular will be fundamental for deciding on the radial height of the baffles and the motor specifications that will be needed to achieve the Rossby and Reynolds numbers of interest, which are at least as high as the current configuration in the 3-m experiment. The enhancement of the flows by a more effective coupling with the inner sphere in both the equatorial and the meridional plane, together with the two different flow topologies observed when adding alpha baffles, seem to be a promising option for our 3-m experiment to effectively increase our chances of obtaining magnetic dynamo action; not only by increasing the radial velocity and the helicity injected into the flow but also by doubling our available parameter space.

ACKNOWLEDGMENTS

We would like to acknowledge helpful conversations with many in the community including H. C. Nataf, A. Tilgner, and K. Moffatt. We gratefully acknowledge support from the National Science Foundation through Grants No. EAR-1417148, No. EAR-1909055, and No. EAR-0116129. Till Zürner acknowledges the Deutsche Forschungsgemeinschaft for Grant No. GRK 1567.

[1] S. Grossmann, D. Lohse, and C. Sun, High–Reynolds number Taylor-Couette turbulence, Annu. Rev. Fluid Mech. **48**, 53 (2016).

[2] S. G. Huisman, D. P. M. van Gils, S. Grossmann, C. Sun, and D. Lohse, Ultimate Turbulent Taylor-Couette Flow, Phys. Rev. Lett. **108**, 024501 (2012).

[3] X. Chavanne, F. Chillà, B. Castaing, B. Hébral, B. Chabaud, and J. Chaussy, Observation of the Ultimate Regime in Rayleigh-Bénard Convection, Phys. Rev. Lett. **79**, 3648 (1997).

[4] G. S. Lewis and H. L. Swinney, Velocity structure functions, scaling, and transitions in high-Reynolds-number Couette-Taylor flow, Phys. Rev. E **59**, 5457 (1999).

[5] D. P. Lathrop, J. Fineberg, and H. L. Swinney, Transition to shear-driven turbulence in Couette-Taylor flow, Phys. Rev. A **46**, 6390 (1992).

[6] T. H. van den Berg, C. R. Doering, D. Lohse, and D. P. Lathrop, Smooth and rough boundaries in turbulent Taylor-Couette flow, Phys. Rev. E **68**, 036307 (2003).

[7] B. Dubrulle and F. Hersant, Momentum transport and torque scaling in Taylor-Couette flow from an analogy with turbulent convection, Eur. Phys. J. B **26**, 379 (2002).

[8] B. Eckhardt, S. Grossmann, and D. Lohse, Torque scaling in turbulent Taylor–Couette flow between independently rotating cylinders, J. Fluid Mech. **581**, 221 (2007).

[9] G. A. Glatzmaiers and P. H. Roberts, A three-dimensional self-consistent computer simulation of a geomagnetic field reversal, Nature (London) **377**, 203 (1995).

[10] A. Kageyama and T. Sato, Computer simulation of a magnetohydrodynamic dynamo. II, Phys. Plasmas **2**, 1421 (1995).

[11] A. Sakuraba and P. H. Roberts, Generation of a strong magnetic field using uniform heat flux at the surface of the core, Nat. Geosci. **2**, 802 (2009).

[12] N. Schaeffer, D. Jault, H.-C. Nataf, and A. Fournier, Turbulent geodynamo simulations: A leap towards Earth's core, Geophys. J. Int. **211**, 1 (2017).

[13] J. Wicht and S. Sanchez, Advances in geodynamo modelling, Geophys. Astrophys. Fluid Dyn. **113**, 2 (2019).
[14] D. S. Zimmerman, S. A. Triana, H.-C. Nataf, and D. P. Lathrop, A turbulent, high magnetic Reynolds number experimental model of Earth's core, J. Geophys. Res.: Solid Earth **119**, 4538 (2014).
[15] E. J. Spence, K. Reuter, and C. B. Forest, A spherical plasma dynamo experiment, Astrophys. J. **700**, 470 (2009).
[16] D. Schmitt, T. Alboussière, D. Brito, P. Cardin, N. Gagnière, D. Jault, and H.-C. Nataf, Rotating spherical Couette flow in a dipolar magnetic field: Experimental study of magneto-inertial waves, J. Fluid Mech. **604**, 175 (2008).
[17] H.-C. Nataf, T. Alboussière, D. Brito, P. Cardin, N. Gagnière, D. Jault, and D. Schmitt, Rapidly rotating spherical Couette flow in a dipolar magnetic field: An experimental study of the mean axisymmetric flow, Phys. Earth Planet. Inter. **170**, 60 (2008).
[18] D. S. Zimmerman, S. A. Triana, and D. P. Lathrop, Bi-stability in turbulent, rotating spherical Couette flow, Phys. Fluids **23**, 065104 (2011).
[19] S. A. Triana, D. S. Zimmerman, and D. P. Lathrop, Precessional states in a laboratory model of the Earth's core, J. Geophys. Res.: Solid Earth **117**, B04103 (2012).
[20] E. C. Bullard and H. Gellman, Homogeneous dynamos and terrestrial magnetism, Philos. Trans. R. Soc., A **247**, 213 (1954).
[21] M. L. Dudley, R. W. James, and P. H. Roberts, Time-dependent kinematic dynamos with stationary flows, Proc. R. Soc. London, Ser. A: Math. Phys. Sci. **425**, 407 (1989).
[22] X. Zhu, R. A. Verschoof, D. Bakhuis, S. G. Huisman, R. Verzicco, C. Sun, and D. Lohse, Wall roughness induces asymptotic ultimate turbulence, Nat. Phys. **14**, 417 (2018).
[23] R. A. Verschoof, X. Zhu, D. Bakhuis, S. G. Huisman, R. Verzicco, C. Sun, and D. Lohse, Rough-wall turbulent Taylor-Couette flow: The effect of the rib height, Eur. Phys. J. E **41**, 125 (2018).
[24] K. Finke and A. Tilgner, Simulations of the kinematic dynamo onset of spherical Couette flows with smooth and rough boundaries, Phys. Rev. E **86**, 016310 (2012).
[25] S. Sanchez, A. Fournier, K. J. Pinheiro, J. Aubert, S. Sanchez, A. Fournier, K. J. Pinheiro, and J. Aubert, A mean-field Babcock-Leighton solar dynamo model with long-term variability, An. Acad. Bras. Ciênc. **86**, 11 (2014).
[26] A. Gailitis, O. Lielausis, E. Platacis, S. Dement'ev, A. Cifersons, G. Gerbeth, T. Gundrum, F. Stefani, M. Christen, and G. Will, Magnetic Field Saturation in the Riga Dynamo Experiment, Phys. Rev. Lett. **86**, 3024 (2001).
[27] R. Stieglitz and U. Müller, Experimental demonstration of a homogeneous two-scale dynamo, Phys. Fluids **13**, 561 (2001).
[28] R. Monchaux, M. Berhanu, M. Bourgoin, M. Moulin, P. Odier, J.-F. Pinton, R. Volk, S. Fauve, N. Mordant, F. Pétrélis, A. Chiffaudel, F. Daviaud, B. Dubrulle, C. Gasquet, L. Marié, and F. Ravelet, Generation of a Magnetic Field by Dynamo Action in a Turbulent Flow of Liquid Sodium, Phys. Rev. Lett. **98**, 044502 (2007).
[29] A. Giesecke, T. Vogt, T. Gundrum, and F. Stefani, Nonlinear Large Scale Flow in a Precessing Cylinder and Its Ability To Drive Dynamo Action, Phys. Rev. Lett. **120**, 024502 (2018).
[30] P. A. Davidson, *An Introduction to Magnetohydrodynamics*, Cambridge Texts in Applied Mathematics (Cambridge University Press, Cambridge, New York, 2001).
[31] H. K. Moffatt, *Magnetic Field Generation in Electrically Conducting Fluids*, Cambridge Monographs on Mechanics and Applied Mathematics (Cambridge University Press, Cambridge, New York, 1978).
[32] S. Childress and A. D. Gilbert, *Stretch, Twist, Fold: The Fast Dynamo*, Lecture Notes in Physics No. m37 (Springer, Berlin, 1995).
[33] T. Nakajima and M. Kono, Kinematic dynamos associated with large scale fluid motions, Geophys. Astrophys. Fluid Dyn. **60**, 177 (1991).
[34] J. X. Love and D. Gubbins, Optimized kinematic dynamos, Geophys. J. Int. **124**, 787 (1996).
[35] I. V. Khalzov, B. P. Brown, C. M. Cooper, D. B. Weisberg, and C. B. Forest, Optimized boundary driven flows for dynamos in a sphere, Phys. Plasmas **19**, 112106 (2012).
[36] R. Holme, Optimised axially-symmetric kinematic dynamos, Phys. Earth Planet. Inter. **140**, 3 (2003).

[37] D. N. Tomin and D. D. Sokoloff, Magnetic field in a fluctuating ABC flow, Astron. Lett. **35**, 321 (2009).
[38] M. Xu, Impact of small scale turbulent flows on dynamo actions, Phys. Lett. A **379**, 577 (2015).
[39] A. P. Willis, Optimization of the Magnetic Dynamo, Phys. Rev. Lett. **109**, 251101 (2012).
[40] D. Holdenried-Chernoff, L. Chen, and A. Jackson, A trio of simple optimized axisymmetric kinematic dynamos in a sphere, Proc. R. Soc. A **475**, 20190308 (2019).
[41] F. Stefani, G. Gerbeth, and A. Gailitis, Velocity profile optimization for the Riga dynamo experiment, in *Transfer Phenomena in Magnetohydrodynamic and Electroconducting Flows: Selected Papers of the PAMIR Conference*, Fluid Mechanics and Its Applications, edited by A. Alemany, P. Marty, and J. P. Thibault (Springer, Dordrecht, Netherlands, 1999), pp. 31–44.
[42] W. Thielicke and E. J. Stamhuis, PIVlab—Towards user-friendly, affordable and accurate digital particle image velocimetry in MATLAB, J. Open Res. Software **2**, e30 (2014).
[43] J. Wicht, Flow instabilities in the wide-gap spherical Couette system, J. Fluid Mech. **738**, 184 (2014).
[44] D. P. Lathrop and C. B. Forest, Magnetic dynamos in the lab, Phys. Today **64** (7), 40 (2011).
[45] P. Linstrom, NIST Chemistry WebBook, NIST Standard Reference Database 69, 1997.
[46] J. Fink and L. Leibowitz, Thermodynamic and transport properties of sodium liquid and vapor, Technical Report No. ANL/RE–95/2, 94649, U.S. Department of Energy Office of Scientific and Technical Information, 1995.
[47] D. J. Tritton, *Physical Fluid Dynamics*, (Oxford University Press, New York, 1988).
[48] M. S. Paoletti and D. P. Lathrop, Angular Momentum Transport in Turbulent Flow between Independently Rotating Cylinders, Phys. Rev. Lett. **106**, 024501 (2011).
[49] H. Schlichting and K. Gersten, *Boundary-Layer Theory* (Springer, Berlin, Heidelberg, 2017).
[50] B. Dubrulle, O. Dauchot, F. Daviaud, P.-Y. Longaretti, D. Richard, and J.-P. Zahn, Stability and turbulent transport in Taylor–Couette flow from analysis of experimental data, Phys. Fluids **17**, 095103 (2005).
[51] D. H. Kelley, S. A. Triana, D. S. Zimmerman, B. Brawn, D. P. Lathrop, and D. H. Martin, Driven inertial waves in spherical Couette flow, Chaos **16**, 1105 (2006).
[52] M. Rieutord, S. A. Triana, D. S. Zimmerman, and D. P. Lathrop, Excitation of inertial modes in an experimental spherical Couette flow, Phys. Rev. E **86**, 026304 (2012).
[53] A. Tilgner, Driven inertial oscillations in spherical shells, Phys. Rev. E **59**, 1789 (1999).
[54] Finke Konstantin, Kinematic dynamo onset and magnetic field saturation in rotating spherical Couette and periodic box simulations, Ph.D. thesis, Georg-August-Universität Göttingen, Göttingen, 2013.
[55] N. Yokoi, Cross helicity and related dynamo, Geophys. Astrophys. Fluid Dyn. **107**, 114 (2013).